AGU PUBLICATIONS

JGR

Journal of Geophysical Research: Space Physics

RESEARCH ARTICLE
10.1002/2015JA021615

Key Points:
- The data-driven 3-D MHD model based on an observed vector magnetograms
- The analysis of the physical properties of a CME
- The morphology of the 3-D simulation result resembles the observations made by STEREO/COR-1

Correspondence to:
S. T. Wu,
wus@uah.edu

Citation:
Wu, S. T., Y. Zhou, C. Jiang, X. Feng, C.-C. Wu, and Q. Hu (2016), A data-constrained three-dimensional magnetohydrodynamic simulation model for a coronal mass ejection initiation, *J. Geophys. Res. Space Physics*, *121*, doi:10.1002/2015JA021615.

Received 10 JUL 2015
Accepted 26 JAN 2016
Accepted article online 28 JAN 2016

A data-constrained three-dimensional magnetohydrodynamic simulation model for a coronal mass ejection initiation

S. T. Wu[1,2], Yufen Zhou[3], Chaowei Jiang[1,3], Xueshang Feng[3], Chin-Chun Wu[4], and Qiang Hu[1,5]

[1]Center for Space Plasma and Aeronomic Research, University of Alabama in Huntsville, Huntsville, Alabama, USA, [2]Department of Mechanical and Aerospace Engineering, University of Alabama in Huntsville, Huntsville, Alabama, USA, [3]SIGMA Weather Group, State Key Laboratory for Space Weather, National Space Science Center, Chinese Academy of Sciences, Beijing, China, [4]Naval Research Laboratory, Washington, District of Columbia, USA, [5]Department of Space Sciences, University of Alabama in Huntsville, Huntsville, Alabama, USA

Abstract In this study, we present a three-dimensional magnetohydrodynamic model based on an observed eruptive twisted flux rope (sigmoid) deduced from solar vector magnetograms. This model is a combination of our two very well tested MHD models: (i) data-driven 3-D magnetohydrodynamic (MHD) active region evolution (MHD-DARE) model for the reconstruction of the observed flux rope and (ii) 3-D MHD global coronal-heliosphere evolution (MHD-GCHE) model to track the propagation of the observed flux rope. The 6 September 2011, AR11283, event is used to test this model. First, the formation of the flux rope (sigmoid) from AR11283 is reproduced by the MHD-DARE model with input from the measured vector magnetograms given by Solar Dynamics Observatory/Helioseismic and Magnetic Imager. Second, these results are used as the initial boundary condition for our MHD-GCHE model for the initiation of a coronal mass ejection (CME) as observed. The model output indicates that the flux rope resulting from MHD-DARE produces the physical properties of a CME, and the morphology resembles the observations made by STEREO/COR-1.

1. Introduction

It is well known that the coronal mass ejection (CME) is one of the major causes of severe space weather events which damage spacecraft and cause orbital degradation. CMEs also elevate the radiation dosage that harm human beings and damage power grids to cause blackouts. Hence, accurate predictions of the geomagnetic storm arrival time (SAT) and strength are essential. Presently, the near-real-time SAT prediction has made significant improvement; however, they still lack accurate predictions of the strength of B_z which is the most important element in prediction of geomagnetic storm strengths. The B_z strength has direct correlation with the strength of the geomagnetic storm [e.g., *Wu and Lepping*, 2015a, 2015b]. The interaction of CMEs of the Earth involves the physical conditions and dynamics of the coupled system including the Sun, solar wind, magnetosphere, ionosphere, and thermosphere. To realistically reflect the three-dimensional (3-D) characteristics of CME propagation and their interaction with the background solar wind [*Wu et al.*, 2007, 2011, 2015; *Liou et al.*, 2014; *Feng et al.*, 2013; *Green and Baker*, 2015; *Wu and Dryer*, 2015], numerical 3-D MHD simulation has become a useful tool for modeling Sun-Earth connection events. A number of 3-D MHD simulations of Sun-Earth connection events have been performed for decades. We may classify these studies according to their CME initiation processes as (i) photospheric converging and shear motion [*Mikić and Linker*, 1994; *Antiochos et al.*, 1994; *Wu et al.*, 2000; *Vourlidas et al.*, 2013] and (ii) flux emergence and cancelation [*Feynman and Martin*, 1995; *Chen and Shibata*, 2000; *Zhang and Wu*, 2009]. In practice, the numerical study of space weather events has used pressure/velocity pulses to represent a CME to simulate the propagation of a CME event [*Groth et al.*, 2000; *Odstrcil and Pizzo*, 2009; *Shen et al.*, 2007; *Wood et al.*, 2012; *Wu et al.*, 2007, 2011, 2015; *Liou et al.*, 2014]. To include the internal CME magnetic structure, there are semitoroidal flux rope models [*Chen et al.*, 1997; *Wu et al.*, 1999; *Manchester et al.*, 2004a, 2004b; *Toth et al.*, 2007; *Cohen et al.*, 2008; *Lugaz et al.*, 2010; *Roussev et al.*, 2004; *Shen et al.*, 2007], magnetized plasma blob models [*Detman et al.*, 1991; *Chane et al.*, 2008; *Shen et al.*, 2011, 2012], and spheromak-type flux rope models [*Vandas et al.*, 1998; *Zhou and Feng*, 2013]. Some of these studies computed the disturbance propagation from near the Sun to 1 AU in a near realistic background solar wind [*Shen et al.*, 2007; *Manchester et al.*, 2008; *Cohen et al.*, 2008; *Lugaz et al.*, 2010; *Zhou et al.*, 2012, 2014; *Zhou and Feng*, 2013]. *Plunkett and Wu* [2000] used a streamer and flux rope model [*Wu et al.*, 1999] to study the January 1997 Sun-Earth connection event. They

showed the difference between simulated and observed storm arrival time, namely, shock arrival time (SAT) was less than 4 h. The dynamic pressure and B_z closely matched the measurements made by *Lu et al.* [1998] and most recently discussed by *Green and Baker* [2015]. The simulation results of *Plunkett and Wu* [2000] were able to produce good agreement with observation because the simulation matches the radial CME velocity as observed by SOHO/Large Angle and Spectrometric Coronagraph up to 30 R_S as presented by *Wu et al.* [1999]. *Wu et al.* [2005] have also performed numerical MHD experiments for three specific driven mechanisms to initiate CMEs using the streamer and flux rope configuration model. They have found that the fast CME could be driven by Lorentz force due to emerging flux at an active region and the slowest CME could be triggered by magnetic buoyancy. All of these CME initiation processes are theoretical which is beneficial to investigate the fundamental physics of CME initiation. In order to construct a prediction model, we have to move to a data-driven approach similar to the meteorological prediction of our terrestrial weather as demonstrated by using an example of space weather forecasting for the 15 February 2011 halo CME [*Webb*, 2013]. In this study, Webb showed that if the input data are continuously updated, the accuracy for the predicted storm arrival time (SAT) could be reached within an hour; however, the lead time for the prediction is rather short (~1 h). But there is one more factor to be considered which is the prediction of the magnitude of B_z at 1 AU such that the internal magnetic structure within the CME has to be taken into account.

In this paper, we will embark on a new approach for three-dimensional magnetohydrodynamic simulation for an active region CME. That is to use a data-driven 3-D MHD active region evolution (MHD-DARE) model to reconstruct a flux rope structure based on the measured vector magnetograms from Solar Dynamics Observatory/Helioseismic and Magnetic Imager (SDO/HMI) [*C.-C. Wu et al.*, 2006; *S. T. Wu et al.*, 2006; *Jiang et al.*, 2013]. Then, this resulting flux rope will be the input for a 3-D MHD global coronal-heliosphere evolution (MHD-GCHE) model developed by *Feng et al.* [2007] to track the propagation and evolution of this observed flux rope structure leading to the launch of a CME. The goal of this investigation is to demonstrate that the observed eruptive flux rope (sigmoid) could initiate a CME which possesses all the observed CME characteristics.

The mathematical description of the models and boundary conditions together with the procedures to integrate these two models will be given in section 2. A brief description of the observation is presented in section 3. The results and discussions are presented in section 4, and the concluding remarks are given in section 5.

2. The Descriptions of the Magnetohydrodynamic Models

Two models are used to implement the present simulation: (i) 3-D MHD data-driven active-region evolution (MHD-DARE) and (ii) 3-D MHD global corona-heliosphere evolution (3-D MHD-GCHE) model. The MHD-DARE model is used to reconstruct the flux rope structure in the source active region near the solar surface, while the MHD-GCHE model is used to simulate the ensuing eruption and evolution of the flux rope from its source region to the solar wind. The numerical method for both models is the Conservation Element and Solution Element (CESE) method [*Feng et al.*, 2007]. The CESE method solves the 3-D governing equations in a substantially different way that is unlike traditional numerical methods (e.g., the finite-difference or finite-volume schemes). The key principle, which is also a conceptual leap of the CESE method, treats space and time as one entity. By introducing the CE and SE to calculate the space-time flux, the CESE method can enforce conservation laws both locally and globally in their natural space-time unity form. In comparison with many other numerical schemes, the CESE method can achieve higher accuracy with the same grid resolution and provide simple mathematics and coding free of any type of Riemann solver or eigen composition. For a more detailed description of the CESE method for MHD simulation including the multimethod control of the well-known $\nabla \cdot \vec{B}$ numerical errors, we refer to our previous works, e.g., *Feng et al.* [2007, 2010, 2014] and *Jiang et al.* [2011]. Since both models have been published [*C.-C. Wu et al.*, 2006; *S. T. Wu et al.*, 2006; *Jiang et al.*, 2013; *Feng et al.*, 2007; *Zhou et al.*, 2012], we will only give a brief description of the two models in the following.

2.1. The 3-D MHD Data-Driven Active Region Evolution Model

Since our interest is focused on the magnetic field and its dynamics with plasma in the low corona where the plasma beta ($\beta = \frac{16\pi nRT}{B^2}$) is very small, we have employed the same numerical model as the MHD equations given in (equation (1)) of *Jiang et al.* [2012] which is designed to reconstruct the quasi-static near-force-free

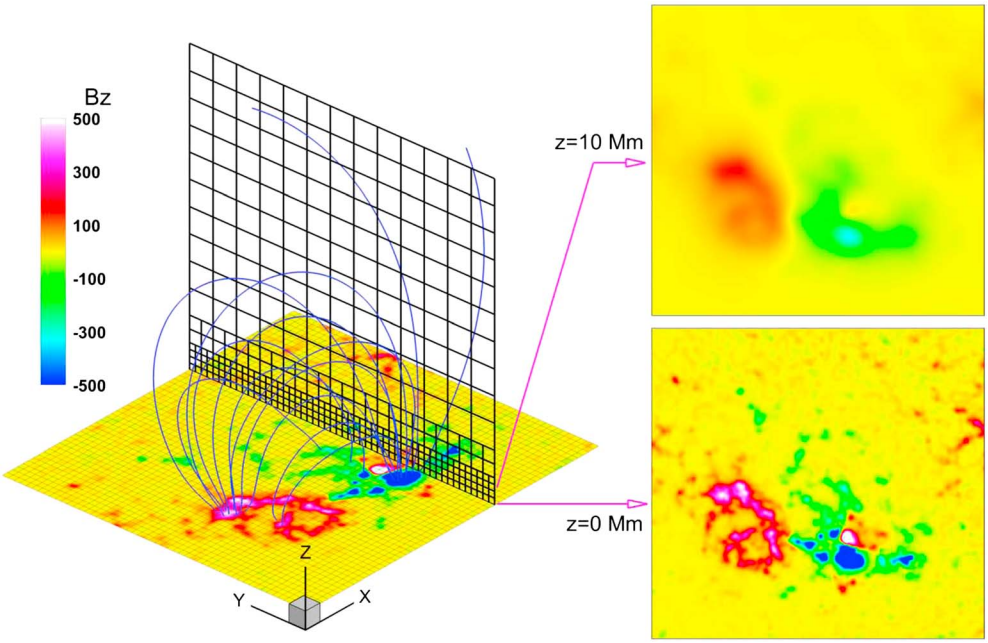

Figure 1. Configuration of the computational grid for AR11283. The entire volume is divided into blocks, and each block has $8 \times 8 \times 8$ cells. (left) Two slices through the volume are plotted to show the structure of the blocks, which are outlined by the black grid lines; the bottom contour map represents B_z of a typical active region on the photosphere, and the curved lines show the potential field lines. (right) The 2-D contour images of B_z sliced at $z = 0$ and $z = 10$ Mm of the potential field model (locations in the 3-D grid are shown by the arrows).

field in the low corona. This set of MHD equations is cast into a Cartesian coordinate system, and the computational volume is at the scale size of an active region. However, because the physical nature of the problem covers a large range of spatial resolution as the magnetic field expands greatly from the bottom (near the photosphere) to the top (high in the corona), the nonuniform grid with the framework of a block-structured distributed-memory parallel computation is used. The grid configuration and its physical resolution are shown in Figure 1. In the horizontal plane (i.e., *x*-*y* plane), the plane parallel to the photosphere, the blocks have the same resolution. Each block consists of $8 \times 8 \times 8$ cells, and the size of each cell is 1 arcsec (about 0.72 Mm). In the vertical direction, block resolution decreases with height, e.g., near the photosphere, the grid spacing matches the resolution of the magnetograms and at the top of the model box, the grid spacing increases 4 times. As can be seen in Figure 1, at a height of about 10 Mm the magnetic field has become far less intermittent, i.e., much smoother than that at the photosphere. Thus, using the nonuniform mesh does not affect the computational accuracy much compared to a uniform mesh but can save significant computational resources.

To initialize the model, a potential field is extrapolated by solving Laplace's equation, $\nabla^2 \phi = 0$, with the bottom boundary condition given by the normal component of the vector magnetogram, $\frac{\partial \phi}{\partial r} = B_z$, which is obtained from HMI on board SDO. Laplace's equation is represented by a large sparse system of linear equations after being discretized on the grid using the finite difference scheme. These equations are solved by the Bi-CGSTAB method [*van der Vorst*, 1992] that is suitable and efficient for such large sparse linear systems. In this way, the derived field ($\vec{B} = \nabla \phi$) will fully match the given boundary map, and the contained information in the map will be preserved. This is unlike eigen function expansion methods that alter the boundary map because of truncation terms. To approximate the low β condition in the low corona, the plasma density on the bottom ρ_0 is assumed to be uniform, with the proton number density given by $n_0 = 1 \times 10^9$ cm^{-3}, and the initial temperature is set to be $T = 0.5 \times 10^6$ K. In a hydrostatic equilibrium, the density is

$$\rho(x, y, z) = \rho_0 \exp\left[-z / \left(\frac{RT(R_s + z)}{g_0 R_s}\right)\right] \quad (1)$$

where R is the gas constant, g_0 is the gravitational constant, and the pressure is given by $p = \rho RT$ and R_S is the solar radius.

After the initial condition is set up, we evolve the system by injecting the observed transverse magnetic field on the bottom. This will drive the system to evolve due to the inconsistency of the potential field with the transverse magnetogram from the observation. We then let the 3-D coronal field relax to a new MHD equilibrium under the condition of a small frictional force.

2.2. The 3-D MHD Global Corona-Heliosphere Evolution Model

To investigate the initial phase of a CME propagation, a 3-D MHD-GCHE model is used for tracking the propagation of a CME from the Sun to Earth or beyond [*Feng et al*., 2007; *Zhou et al*., 2012, 2014; *Zhou and Feng*, 2013]. The 3-D MHD governing equations consist of conservation for mass, momentum, magnetic induction, and energy, which is identical to those equations (i.e., equation (1)) given by *Feng et al*. [2007] and *Feng et al*. [2010]. In order to reproduce the observed pattern of fast and slow solar winds, the heating term is defined by $S_E = Q_0 \cdot \frac{1}{f_s} \exp(-r/L_Q)$, where the constant value $Q_0 = 1.0 \times 10^{-6}\,\mathrm{J\,m^{-3}\,s^{-1}}$, and the decay length of heating L_Q is set to be $0.9\,R_S$. The expansion factor $f_s = \left(\frac{R_s}{r}\right)^2 \frac{B_{Rs}}{B_r}$, where B_{R_s} is a magnetic field at the solar surface, and r is the distance from the solar center. This model was tested using the 4 November 1997 CME event [*Zhou et al*., 2012] and showed that the model is able to predict the B_z quite well at 1 AU as verified by Wind spacecraft measurements.

In the MHD-GCHE model, for the study of propagation of solar disturbances (i.e., CME) the background solar wind is very important [*C.-C. Wu et al*., 2006; *S. T. Wu et al*., 2006]. Thus, the first step is to construct a quasi-steady solar wind using the observed photospheric line-of-sight magnetic field and Parker's 1-D solar wind solution as the trial values. The temperature and density at the inner boundary (at $1\,R_S$) are typically taken to be $T = 1.7 \times 10^6$ K and $\rho_s = 1.67 \times 10^{-13}\,\mathrm{kg\,m^{-3}}$, respectively. The magnetic field is split into two parts (i.e., $\vec{B} = \vec{B}_0 + \vec{B}_1$), where $\vec{B}_0$ is a potential magnetic field obtained by the potential field source surface model [e.g., *Luhmann et al*., 2002] based on the observed photospheric line-of-sight magnetic field from the Wilcox Solar Observatory (WSO) at Stanford University. We understand that the resolution of the WSO magnetograms is rather low; thus, it may miss some information about the overlying coronal field. Thus, the high-resolution magnetograms such as HMI will be used for the further study. The computational domain covers $0° \le \theta \le 180°$, $0° \le \phi \le 360°$, and $1\,R_S \le r \le 3\,R_S$. Like the MHD-DARE model, the 3-D MHD-GCHE model for CME propagation is constructed using nonuniform grid with the framework of a block-structured distributed-memory parallel computation. During the calculation, five levels of grid refinement are used to obtain a grid cell size of $0.005\,R_S$ near the active region. Indeed, due to the large amount of computation and the limitation of computational conditions, the resolution in the global model is not high enough compared with the SDO/HMI data. The details of the computing background solar wind were given previously [*Feng et al*., 2007; *Hu et al*., 2008; *Feng et al*., 2010, 2011, 2014] and thus not repeated here.

Since the problems we have encountered cover a range from subsonic/sub-Alfvénic to supersonic/super-Alfvénic, thus, the method of projected characteristics [*Wu and Wang*, 1987] is employed for this study at the bottom boundary where it is possible to self-consistently implement the time-dependent measurements (i.e., photosphere). In such a treatment, the subphotosphere (i.e., convection zone) information can be reflected to the corona and beyond by following these characteristics, because the photospheric measurements contain the convection zone effects. Specific mathematic expressions of these boundary conditions are given by *C.-C. Wu et al*. [2006] and *S. T. Wu et al*. [2006] for Cartesian coordinates and spherical coordinates [*Wang et al*., 2011; *Yang et al*., 2012], respectively. The boundary conditions for the lateral and top sides are set by the nonreflective boundary conditions.

3. Observations

To illustrate the composite three-dimensional magnetohydrodynamic Sun-Earth simulation model, we have selected AR11283 for demonstration. AR11283 at N14W18 is one of the very productive active regions (ARs) in the new solar cycle, producing several major flares/CMEs around the disk center from 4 to 7 September 2011. Figure 2 shows the measured evolution of the photospheric vector magnetic field from SDO/HMI during the period 4–6 September 2011. Initially, this region had a simple bipolar configuration as a mature AR (4 September 2011), with a leading negative-polarity sunspot (N0) and trailing positive polarity (P0) that appears much more dispersed. Then, a new bipolar field (labeled as P1/N1) emerges west of the preexisting negative polarity (N0), forming a delta sunspot group. The newly emerging polarities move apart quickly from

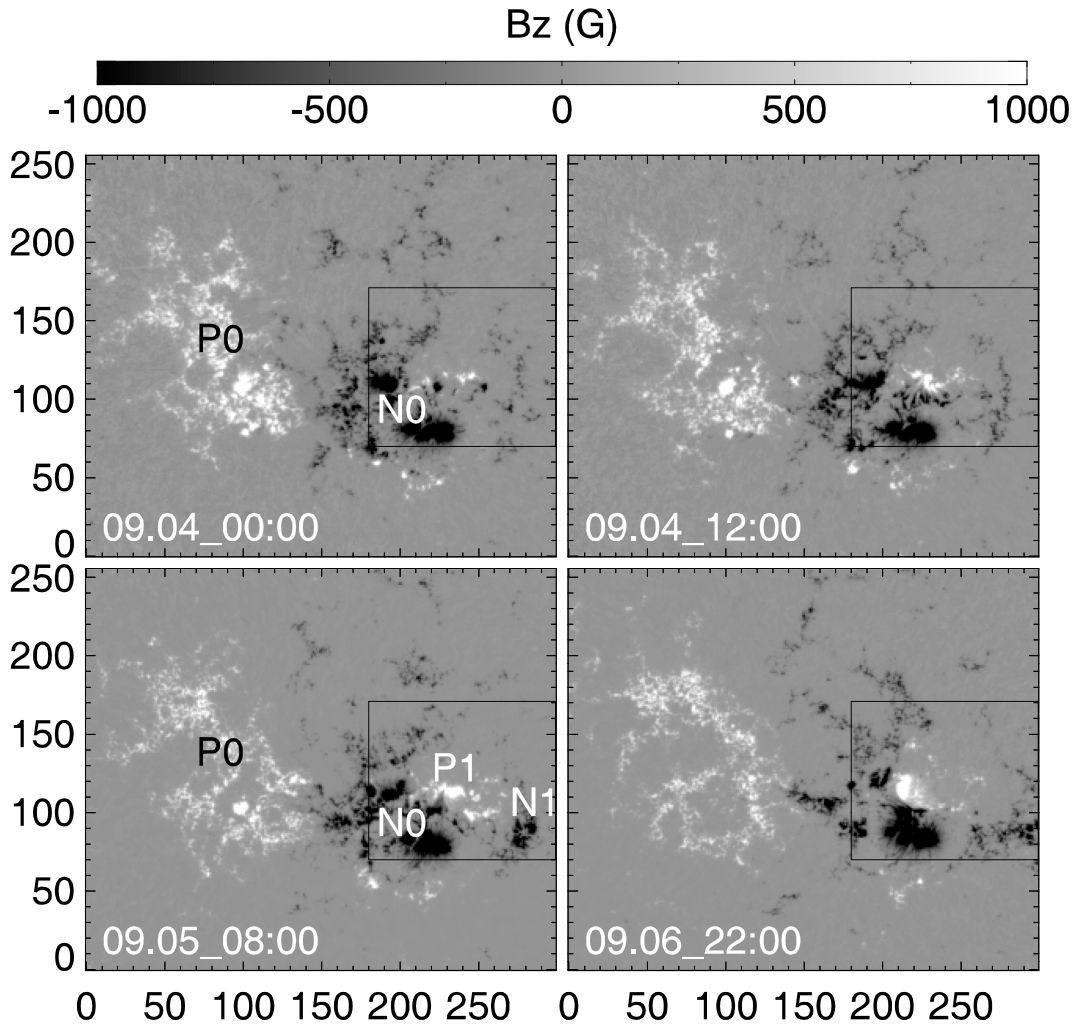

Figure 2. Evolution of the vector magnetograms obtained by SDO/HMI of AR11283 from 4 to 6 September 2011. Four snapshots are shown. The black box outlines the region of the flux emergence and eruption. P0/N0 labels the preexisting polarities and P1/N1 the new emerging polarities. The length unit is arcsec [*Jiang et al.*, 2014b].

each other as usually observed in flux emergence sites, and N1 approaches the west boundary of the magnetogram. It is worth noting that the positive P1 is surrounded by negative flux, indicating that a coronal null point is likely formed above. After the initial stage of flux emergence with the apparent new flux injection completed, rotation of P1 and shearing motion between P1/N0 are observed. Such photospheric motions make a continuous injection of magnetic free energy and helicity into the corona causing the eruption as observed as shown in Figure 3 from the images obtained by SDO/ Atmospheric Imaging Assembly (AIA) in various channels. By examining these images, it is clear that the buildup of this region begins at 00:00 UT on 4 September 2011, then eruption starts at 22:00 UT, 6 September 2011. The simulation focuses on the flux emergence and eruption region as indicated by the black box shown in Figure 2. There was a resulting CME observed in the lower corona by STEREO/COR-1 on 6 September 2011.

4. Numerical Results and Discussions

4.1. Insertion of Observed Flux Rope Structure (Sigmoid)

To implement this study, the first step is to construct a flux rope structure based on the measured vector magnetograms from SDO/HMI. *Jiang et al.* [2014a, 2014b] have presented a result of the formation and eruption of an observed sigmoid (flux rope) in AR11283 during the period of 6 September 2011 as shown in Figure 4 by input of observed vector magnetograms obtained by SDO/HMI at 22:00 UT 6 September

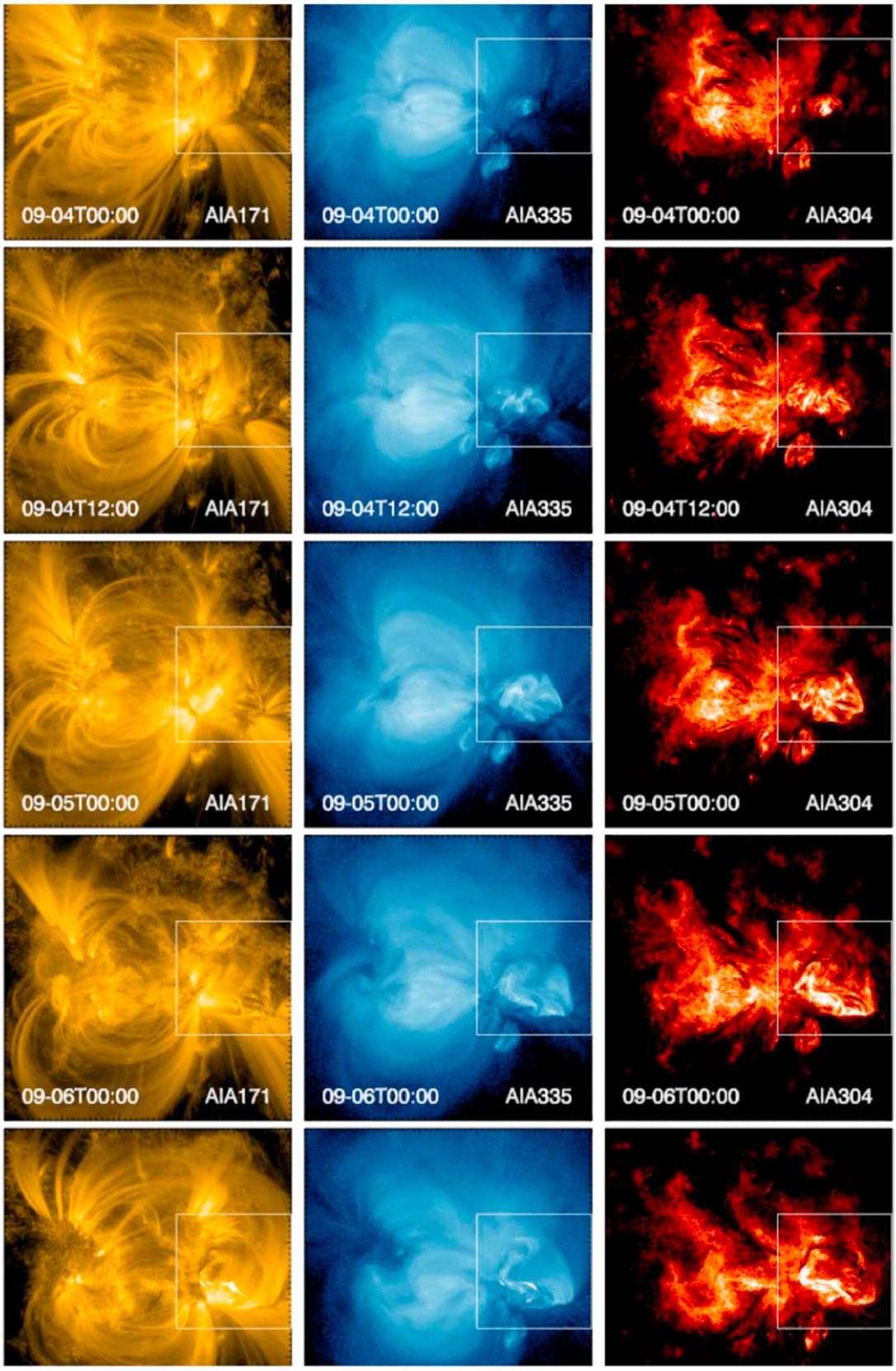

Figure 3. Evolution of the AR observed in different AIA channels; the boxes outline the flux emergence site, and the eruption is beginning to build up at 4–6 September 2011. The major eruption is around 6 September 2011 at 22:00 UT [*Jiang et al.*, 2014b].

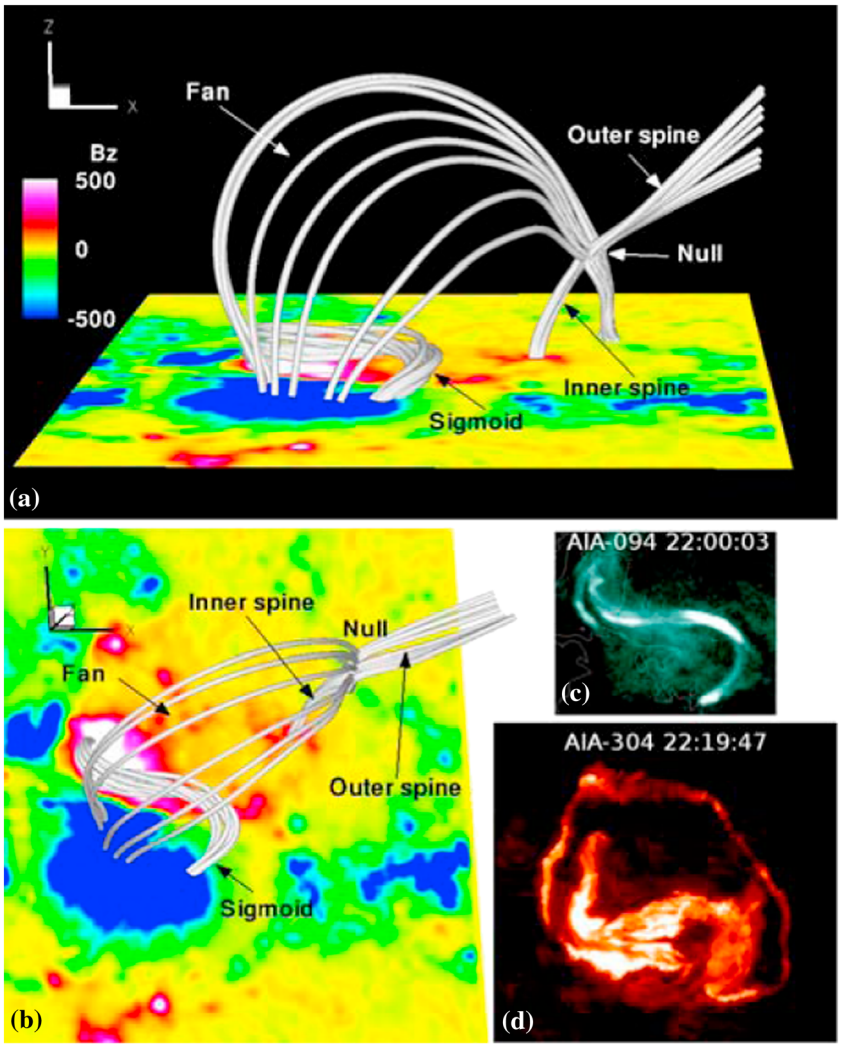

Figure 4. Magnetic topology simulated by nonlinear force-free field model before the eruption (6 September 2011 22:00 UT). The sigmoid field is the low-lying S-shaped lines; field lines touching the null outline the spine-fan topology of the null, where the lines form an X-point configuration. The null point locates ~18 arcsec (13 Mm) above the photosphere and ~50 arcsec away from the sigmoid in the same direction of the eruption. (a) A side view and (b–d) the SDO view. Compared with Figure 4b are the sigmoid observed by SDO/AIA-94 channel and the circular flare ribbon observed by AIA-304 [*Jiang et al*., 2013].

2011 before the eruption. The upper panel shows the side view magnetic topology of the simulated sigmoidal flux rope field (the low-lying S-shaped lines) covered by the ambient low coronal field. The field lines touching the null outline the spine-fan topology of the null where the field forms an X-point configuration. Figure 4b is the vertical view similar to the SDO view which matches well with the sigmoid observed by SDO/AIA-94 channel (Figure 4c) and the circular flare ribbon observed by AIA-304 channel (Figure 4d). We will use these results as the input to the 3-D MHD-GCHE model for the investigation of the CME initiation. To insert this solution into the 3-D MHD-GCHE model, the following interpolation algorithm from the 3-D MHD-DARE grid to the 3-D MHD-GCHE grid is adopted:

$$B_{(r,\theta,\varphi,t)}{}^{\mathrm{MHD}}\left(r_i,\theta_j,\varphi_k,t\right) = B_{(r,\theta,\varphi,t)}{}^{\mathrm{FR}}(r_0,\ \theta_0,\ \varphi_0,\ t) + \nabla B_{(r,\theta,\varphi,t)}{}^{\mathrm{FR}}\cdot\nabla\ \vec{s}\quad + \frac{1}{2}\left|H^{\mathrm{FR}}(r_0,\ \theta_0,\ \varphi_0,\ t)\right|\nabla s^2 \qquad (2)$$

where the $\vec{B}^{\mathrm{FR}}$ represents the flux rope magnetic field at the 3-D MHD-DARE model grid and the $\vec{B}^{\mathrm{MHD}}$ represents the magnetic field of the 3-D MHD-GCHE model grid. These two grids have a different number of points and different spacing. The $(r_i, \theta_j, \varphi_k)$ are the indices identifying the position at the 3-D MHD-GCHE model, and $B_{(r,\theta,\varphi)}$ $(r_0, \theta_0, \varphi_0)$ are the values of the components of the $\vec{B}^{\mathrm{FR}}$ closest to the coordinates of the point $(r_i, \theta_j, \varphi_k)$

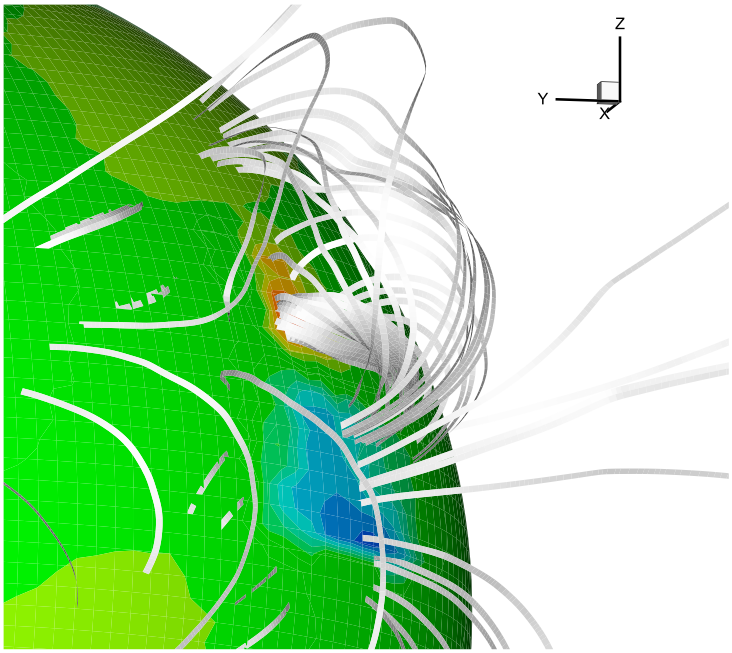

Figure 5. Three-dimensional view of the initial magnetic field 3-D MHD-GCHE model resulting from insertion of the observed flux rope of AR11283, 6 September 2011 22:21:35 UT. The color contours represent the radial magnetic field strength on the solar surface.

and $\Delta s = (\mathrm{d}r, r\mathrm{d}\theta, r\sin\theta\,\mathrm{d}\varphi)$. The adjacent cells are used to compute the gradients of the components of the magnetic field $\nabla B_{(r,\theta,\varphi)}{}^{\mathrm{FR}}$ and the Hessian matrix $|H^{\mathrm{FR}}(r_0, \theta_0, \varphi_0)|$ through finite differences. The second-order interpolation is performed to guarantee a correct transformation of the spatial derivations of magnetic field between the two models and thus the Lorentz force. This procedure is the same as done by *Pagano et al.* [2013]. Figure 5 shows the flux rope (sigmoid) present in the 3-D MHD-GCHE model after the inclusion of the preeruption flux rope structure (at 22:21:35 UT on 6 September 2011) obtained by the 3-D MHD-DARE as shown in Figure 4. It is obvious that the flux rope configuration is preserved. The Alfvénic and fast mode wave speed of the background corona based on measured line-of-sight magnetic field on 6 September 2011 is presented in Figure 6. It is clearly noted that the fast mode MHD wave is almost identical to the Alfvénic speed. This is theoretically expected for low beta plasma [*C.-C. Wu et al.*, 2006; *S. T. Wu et al.*, 2006, see Appendix], and the coronal flow (early stage of the solar wind) is in the order of tenths km/s. This very slow speed solar wind is due to the given source term for solar wind acceleration that begins taking effect beyond $2\,R_S$. In what follows, we will track the evolution of this flux rope structure in the lower corona and investigate whether the properties possess the characteristic of a CME. By evaluating the decay index of the overlying field that stabilizes the flux rope [*Jiang et al.*, 2014a, 2014b], we found this simulated flux rope magnetic field configuration is subject to torus instability (TI) [*Kliem and Török*, 2006]. Such an unstable nature of the pre-eruptive field is also confirmed by a test using an ideal MHD simulation with the flux rope as the initial condition, which shows that it erupts and matches the AIA images well in morphology as shown by *Jiang et al.* [2013] and *Wu et al.* [2013]. Hence, we will input this realistic unstable flux rope into the 3-D MHD-GCHE model for the CME initiation.

4.2. CME Morphology and Propagation

The evolution of this flux rope and its interaction with the solar wind in the lower corona is depicted in Figure 7 at 4 times. It is clearly noticed that there are three parts of the magnetic field structure which are as follows: (i) flux rope (sigmoid), (ii) the overlying fields covering the flux rope to keep the flux rope in equilibrium with the ambient structure, and (iii) the magnetic field of the solar wind. The magnetic field of types (i) and (ii) resulted from the active region magnetic field deduced from the vector magnetograms obtained by SDO/HMI. The solar wind field is constructed using the observed line-of-sight field together with the 3-D MHD-GCHE model. Examining Figure 7 clearly shows the flux rope moving upward due to the torus

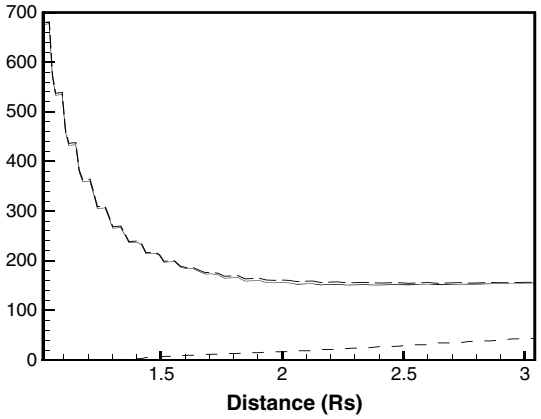

Figure 6. The background radial velocity (dashed line), Alfven wave speed (solid line), and fast wave speed (long dashed line) at N14W18 with units km/s versus distance.

instability as discussed by *Jiang et al.* [2014a, 2014b] with an estimated average speed of approximately 718 km/s as shown in Table 1. The average speed deduced from COR-1 five point data is 726 km/s. Thus, our simulation matches the COR-1 measurement well. In order to quantitatively examine the evolution of the field topology, we have plotted magnetic field strength and plasma density in 2-D (i.e., r-θ plane) distributions of these quantities at the meridional plane (i.e., $\varphi = 18°$) in Figure 8. Some interesting features can be noted in Figure 8. That is the horn-shaped feature which corresponds to the unevenly twisted field as shown by *Jiang et al.* [2013] and *Wu et al.* [2013] as projected in 2-D meridional plane. This horn-shaped feature gradually evens-out, as it propagates outward to result in a lateral expansion of the CME as usually observed. Another important feature is the development of a high-density region at the interface between the solar wind field (open field) and the active region sigmoid field which could be the source of a solar energetic particle (SEP) event because the high-energy particles easily escape to follow the solar wind open field lines to

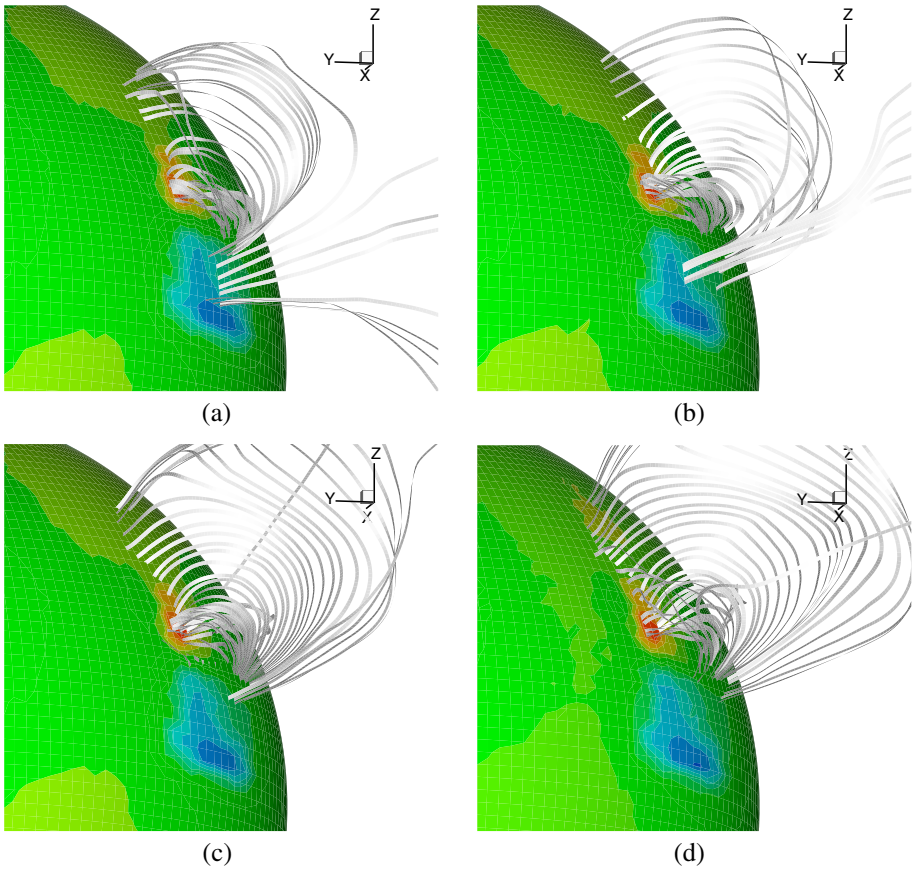

Figure 7. Time evolution of the 3-D representation of a flux rope CME magnetic field for 6 September 2011 at (a) t = 22:23:35 UT, (b) t = 22:25:35 UT, (c) t = 22:27:35 UT, and (d) t = 22:29:35 UT. The color on the solar surface represents the B_r strength.

Table 1. The Distance and Radial Velocity of Several Features as a Function of Time for 6 September 2011 STEREO/COR-1 Measurements and the Corresponding Simulation Results

			Simulation			
STEREO/COR-1 Measurements			Distance (R_S)		Radial Velocity (km/s)	
Time (UT)	Distance (R_S)	Radial Velocity (km/s)	Shock Front	Flux Rope Front	Shock Front	Flux Rope Front
22:23:35	-		1.44	1.17		
22:25:18	1.58		-	-	-	-
22:25:35	-		1.52	1.29	463.33	695.00
22:27:35	-		1.68	1.43	926.67	810.83
22:28:35	-		1.76	1.48	926.67	868.75
22:30:18	1.86	630	-	-		
22:35:18	2.17	697.5	-	-		
22:40:18	2.48	697.5	-	-		
22:45:18	2.87	877.5	-	-		
Average Speed		725.63			741.33	718.17

reach the Earth. The location of this high-density region propagates outward, and its corresponding Mach number of the fast mode as a function of time is shown in Figure 9. By examining these two curves together, we recognize that the flow becomes supersonic and super-Alfvénic at ~1.5 R_S. The compression ratio $\left(\frac{\rho-\rho_0}{\rho_0}\right)$ shown in Figure 8 has increased from 0.74 to 3.87 due to shock compression. Figure 10 shows a distance-time curve for the shock front and flux rope front; it also shows that the fast shock appears at ~ 1.4 R_S. This is consistent with the results shown in Figure 9 but has a small discrepancy which is caused by numerical accuracy in tracking the shock front. This shock is a piston-driven shock, and the flux rope is acting as the piston. The quantitative comparison between the STEREO/COR-1 measured and simulated CME kinematics is given in Table 1. Based on this comparison, the simulation matches very well to the observation in which the simulated shock front matches the COR-1 CME front as indicated by the asterisks shown in Figure 10.

Figure 11 shows the simulated polarization brightness (pb) image from 1.2 R_S in comparison with COR-1 images for 6 September 2011 at 22:25:18 UT and 22:30:18 UT, respectively. The simulated pb brightness image is produced as follows. A satellite position is defined, as well as the direction in which it is looking. The plane-of-sky is defined as the plane perpendicular to the particular line of sight joining the Sun and the satellite. For each point of the image, the line of sight passing through this point and the satellite is defined, and the density is calculated at discrete locations along this line. Then the pb brightness is calculated using a formula from *Billings* [1966]. The COR-1 images are very faint. Examining the simulated images clearly shows the classical three parts of coronal mass ejection: (i) a bright front, (ii) a dark cavity, and (iii) a bright compact core. Since the bright front is shown at a distance larger than 1.85 R_S; thus, it is identified as a shock according to Figure 9. The strength of this shock could be estimated from Figure 9, where the fast mode Mach number is larger than 1.9. Presence of a fast-mode shock at this height has a profound implication to the generation of solar energetic particles (SEPs). It has been long argued that CME-driven shocks are the acceleration site of gradual SEP events [e.g., *Reames*, 1999]. All ground level enhancement (GLE) events in Solar Cycle 23 have been found to be caused by large and fast CMEs [*Li et al*., 2012]. Indeed, the release height of these energetic particles in GLE events is found to be of only a few solar radii [*Reames*, 2009]. From our simulation we can see that a CME-driven shock can form as low as ~1.5 R_S. Furthermore, there are also open field lines threaded through the CME-driven shock front. Therefore, it is conceivable that particles can be accelerated to high energies at this height and then propagate to 1 AU along the open field lines. Of course, the detailed particle acceleration process depends on a variety of shock parameters including shock compression ratio, shock geometry, and wave intensity near the shock front. [*Zank et al*., 2000; *Li et al*., 2003, 2005, 2009]. It was found that there is a good linear relationship between the logarithmic flux of oxygen SEPs ($E > \sim 10\,\mathrm{MeV\,n^{-1}}$) observed by the ACE spacecraft and the Mach numbers of concurrent simulated (1.5-D) fast mode shocks [*Liou et al*., 2012, 2013]. A recent study of the CME event on 15 March 2013 also showed that there is a good linear relationship between the logarithmic of time-intensity profile of SEPs and the concurrent (3-D) simulated fast-mode shock Mach number [*Wu et al*., 2015]. The dark region behind the shock in the simulation is the flux rope. There are two parts of the dark region due to the complexity of

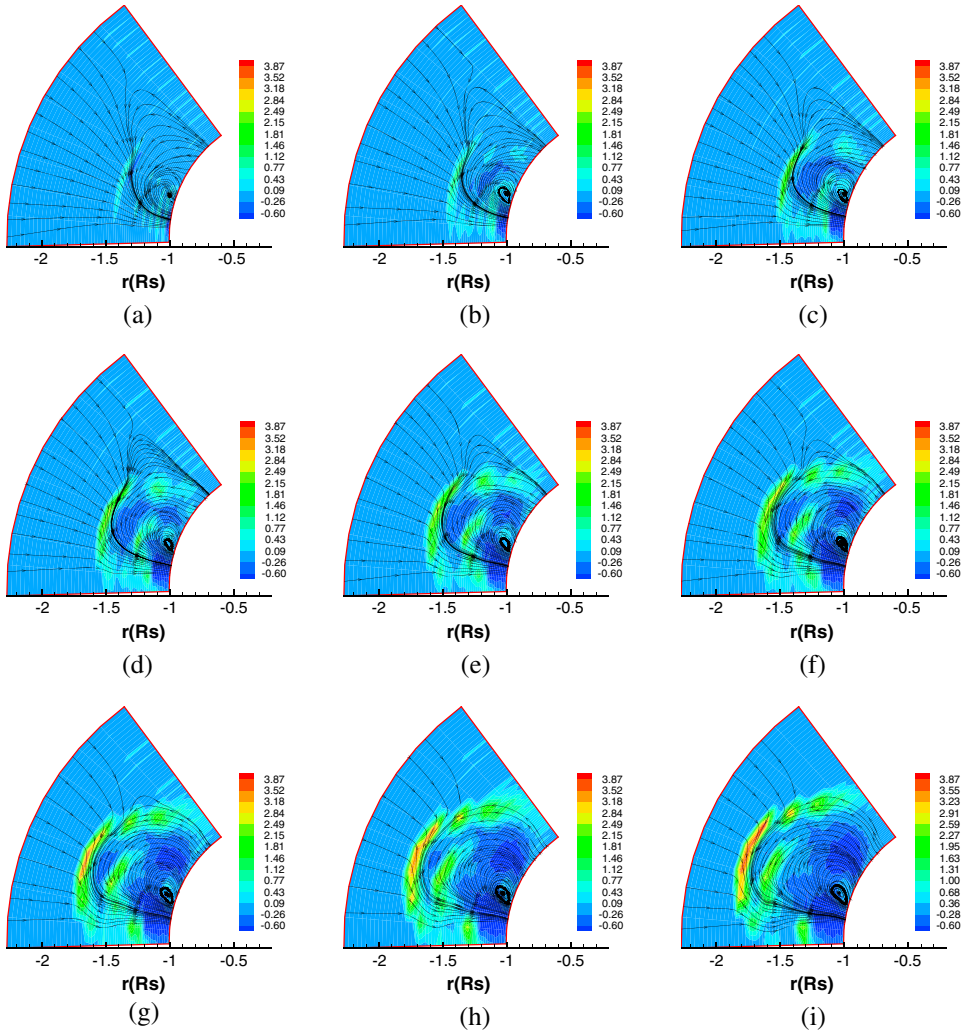

Figure 8. Time evolution of the CME in the r-θ plane for 6 September 2011 at (a) $t = 22{:}22{:}35$ UT, (b) $t = 22{:}23{:}35$ UT, (c) $t = 22{:}24{:}35$ UT (d) $t = 22{:}25{:}35$ UT, (e) $t = 22{:}26{:}35$ UT, (f) $t = 22{:}27{:}35$ UT, (g) $t = 22{:}28{:}35$ UT, (h) $t = 22{:}29{:}35$ UT, and (i) $t = 22{:}30{:}35$ UT. The background color represents the density ratio $\left(\frac{\rho - \rho_0}{\rho_0}\right)$ as indicated by the color bar.

the magnetic flux distribution shown in Figure 7. By examining Figure 8 further, we notice that the center of the flux rope moves much slower than the flux rope front because the center region contains a large amount of mass which is subject to gravitational pull. On the other hand, the flux rope front develops a fast expansion due to the relaxation of the magnetic field configuration.

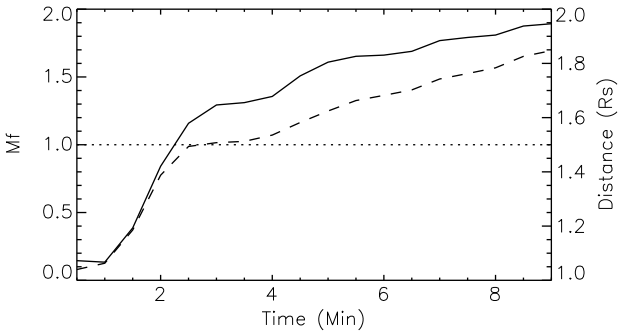

Figure 9. The evolution of maximal relative density front (dashed line) and the corresponding evolution of fast magneto-acoustic speed Mach number (solid line) versus time for 6 September 2011.

4.3. CME Energetics

Since the revealed flux rope is unstable due to the torus instability (TI); thus the simulated CME is caused by torus instability of the flux rope in the corona. Consequently, the amount of energy comes from the preevent coronal initial state with an embedded flux rope which consists of energy from the active region flux rope and background solar wind. Based on these facts, we have

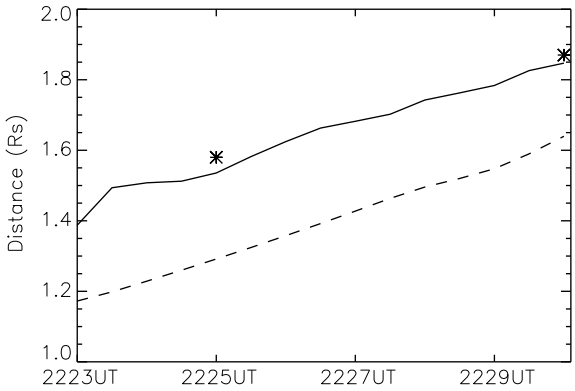

Figure 10. The evolution of shock front (solid line), flux rope front (dashed line) versus time on 6 September 2011, where asterisk indicates the corresponding COR-1 observation.

estimated a maximum total energy of $\sim 1.97 \times 10^{32}$ ergs which contain 10^{31} ergs kinetic energy, 1.2×10^{31} ergs thermal energy, 3.5×10^{31} ergs potential energy, and 1.4×10^{32} ergs magnetic energy. The majority of the energy is coming from the flux rope. It is obvious that this flux rope-initiated CME is magnetically driven.

5. Concluding Remarks

We have successfully initiated a CME by using an observed twisted metastable flux rope (sigmoid) structure and by integrating a 3-D MHD-DARE model and a 3-D MHD-GCHE model to form a composite Sun-Earth simulation model. The 3-D MHD-DARE model provides us the ability to reveal the active region twisted flux rope structure using vector magnetograms as the input, then this deduced twisted flux rope is inserted into the 3-D MHD-GCHE model, for a CME initiation. The simulated observed twisted flux rope is subject to the torus instability as indicated by the decay index [*Jiang et al*., 2014a, 2014b]. This flux rope

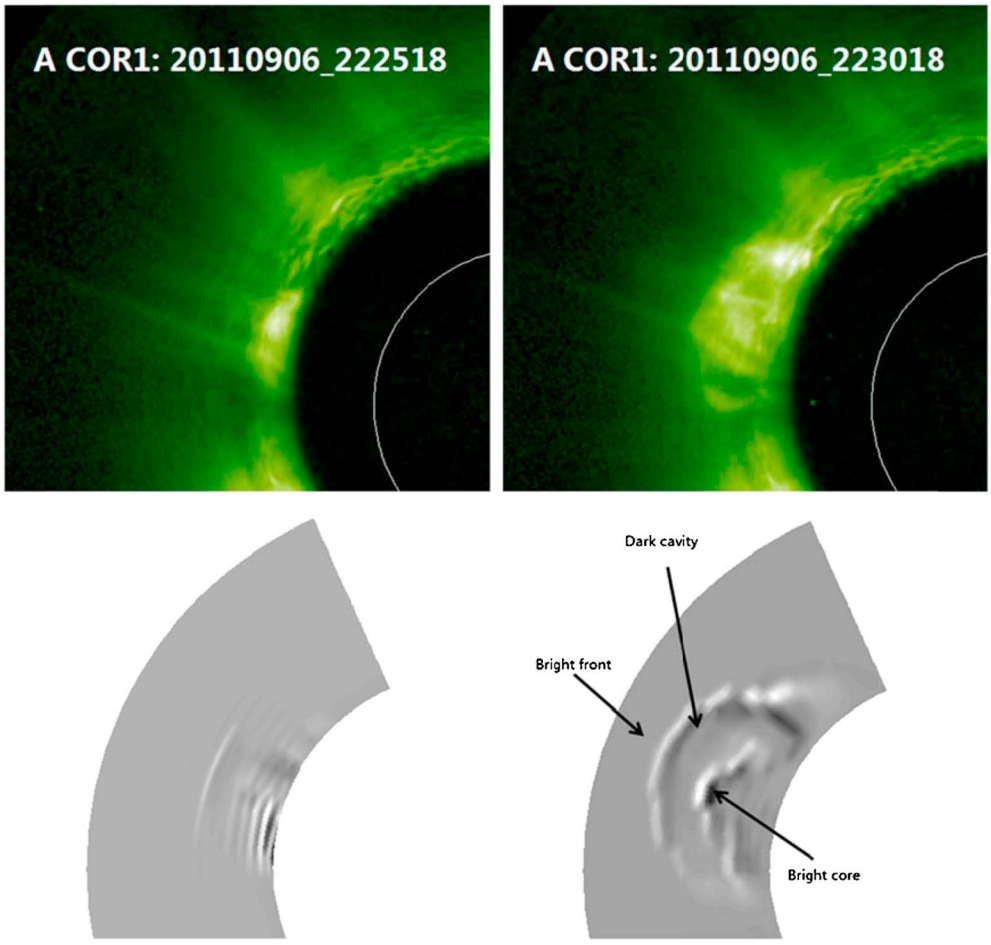

Figure 11. (bottom) The simulated pb brightness image in comparison with (top) COR-1 images for 6 September 2011 at 22:25:18 UT and 22:30:18 UT.

erupts and interacts with the ambient solar wind. This CME is magnetically driven, as we have estimated based on the CME energetics. Physically, this CME is caused by the emerging flux of an active region as shown in Figure 2. Subsequently, it generates a flux rope (sigmoid) structure. This flux rope core becomes unstable and leads to the initiation of a CME. In fact, this simulation of CME initiation is similar to the initiation process done by *Manchester et al*. [2004a, 2004b], but they used a theoretical flux rope model given by *Gibson and Low* [1998]. Several interesting features are described as follows:

1. From the simulation of the magnetic topology shown in Figure 7, we notice that there are three parts of the magnetic structure (1) twisted flux rope (sigmoid), (2) the magnetic field draping the flux rope to keep the flux rope in equilibrium within the active region, and then we can observe (3) the solar wind field. The first two parts are the magnetic fields in the active region, and the third is the solar wind field.
2. We revealed a location that should be favorable to the origination of a solar energetic particle (SEP) event, as shown in Figure 8. The location is at the interface between the active region field (i.e., flux rope and its ambient field) and the open field of the solar wind. Because of the limited computer resources, this simulation is limited to the region of COR-1.
3. A fast-mode MHD shock develops as low as ~1.5 R_S. This has also been observed in our previous study of the propagation of extreme ultraviolet imaging telescope waves [*Wu et al*., 2001]. This piece of knowledge is worth noting because of the anticipated launch of the Solar Probe Plus (SPP) mission.
4. The simulated CME energetics closely resembles a typical CME.
5. The timing of the simulated CME matches the COR-1 observation pretty well as shown in Table 1. The front of the observed CME corresponds to the simulated shock front and closely resembles the high-density region as shown in Figures 9 and 10.

It is worth noting that this simulation of the initiation of the CME is quite different from other current models. This model uses an observed unstable flux rope as the initiation of a CME. As a final remark, we need not only to extend this simulation to Earth's environment (i.e., 1 AU) to achieve a space weather prediction model but also to use a sequence of magnetograms to drive the model as in our previous active region evolution study [*C.-C. Wu et al*., 2006; *S. T. Wu et al*., 2006]. These results will be compared to in situ data for verification of this three-dimensional magnetohydrodynamic Sun-Earth simulation model. Eventually, this model will be used to connect all the Sun-Earth system observations including SDO, SPP, STEREO, ACE, and Wind measurements. Coupling our CME initiation and propagation MHD code with a particle acceleration model is also a promising topic requiring future consideration.

Acknowledgments

Work performed by S.T.W., C.W.J., and Q.H. is supported by NSF grant AGS-1153323. Y.F.Z. and X.S.F. are supported by the National Basic Research Program of China (grant 2012CB825601) and the National Natural Science Foundation of China (41231068, 41374176, 41574171, and 41531073). Work of C.C.W. is supported by Chief of Naval Research. Q.H. also acknowledges NSF grant AGS-1062050 for partial support. You may obtain the data by contacting Yufen Zhou at yfzhou@spaceweather.ac.cn. The numerical calculation has been completed on our SIGIMA Cluster computing system. Data are courtesy of NASA/SDO and WSO, HMI, and STEREO/COR-1 science teams. The authors would like to express their appreciation to Simon Plunkett and Gang Li for reading the manuscript and giving invaluable suggestion. In addition, we thank the referees for their comments for improving the manuscript.

References

Antiochos, S. K., R. B. Dahlburg, and J. Klimchuk (1994), The magnetic field of solar prominences, *Astrophys. J. Lett.*, *420*, L41–44.

Billings, D. E. (1966), *A Guide to the Solar Corona*, Academic Press, New York.

Chane, E., S. Podts, and B. Van der Holst (2008), On the combination of ACE data with numerical simulation to determine the initial characteristics of a CME, *Astron. Astrophys.*, *492*, L29–L32.

Chen, J. R., A. Howard, and G. E. Breckner (1997), Evidence of an erupting magnetic flux rope: LASCO coronal mass ejections of 1997 April 13, *Astrophys. J.*, *409*, L191–L194.

Chen, P. F., and K. Shibata (2000), An emerging flux trigger mechanism for coronal mass ejections, *Astrophys. J.*, *545*, 524–531.

Cohen, O., I. V. Sokolov, I. I. Roussev, N. Lugaz, W. B. Manchester, T. I. Gombosi, and C. N. Arge (2008), Validation of a global 3D heliospheric model with observations for the May 12, 1997 CME event, *J. Atmos. Sol. Terr. Phys.*, *70*, 583–592.

Detman, T. R., M. Dryer, T. Yeh, S. M. Han, S. T. Wu, and D. J. McComas (1991), A time-dependent, three-dimensional MHD numerical study of interplanetary magnetic draping around plasmoids in the solar wind, *J. Geophys. Res.*, *96*(A6), 9531–9540, doi:10.1029/91JA00443.

Feng, X. S., Y. F. Zhou, and S. T. Wu (2007), A novel numerical implementation for solar wind modeling by the modified conservation element/solution element method, *Astrophys. J.*, *655*, 1110–1126.

Feng, X. S., L. P. Yang, C. Q. Xiang, S. T. Wu, Y. F. Zhou, and D. K. Zhong (2010), Three-dimensional solar wind modeling from the Sun to Earth by a SIP-CESE MHD model with a six-component grid, *Astrophys. J.*, *723*, 300–319.

Feng, X. S., S. H. Zhang, C. Q. Xiang, L. P. Yang, C. W. Jiang, and S. T. Wu (2011), A hybrid solar wind model of the CESE + HLL method with a Yin-Yang overset grid and an AMR grid, *Astrophys. J.*, *734*(1), 50.

Feng, X. S., C. Q. Xiang, and D. K. Zhong (2013), Numerical study of interplanetary solar storms [in Chinese], *Sci. Sin. Terrae*, *43*, 912–933.

Feng, X. S., C. Q. Xiang, D. K. Zhong, Y. Zhou, L. Yang, and X. Ma (2014), SIP-CESE MHD model of solar wind with adaptive mesh refinement of hexahedral meshes, *Comput. Phys. Commun.*, *185*, 1965–1980.

Feynman, J., and S. F. Martin (1995), The initiation of coronal mass ejections by newly emerging magnetic flux, *J. Geophys. Res.*, *100*(A3), 3355–3367, doi:10.1029/94JA02591.

Gibson, S., and B. C. Low (1998), A time-dependent three-dimensional magnetohydrodynamic model of the coronal mass ejection, *Astrophys. J.*, *493*, 460–473.

Green, L., and D. Baker (2015), Coronal mass ejections: A driver of severe space weather, *Weather*, *70*, 31–35.

Groth, C. P. T., D. L. DeZeeuw, T. I. Gombosi, and K. G. Powell (2000), Global three-dimensional MHD simulation of a space weather event: CME formation, interplanetary propagation, and interaction with the magnetosphere, *J. Geophys. Res.*, *105*(A11), 25,053–25,078, doi:10.1029/2000JA900093.

Hu, Y. Q., X. S. Feng, S. T. Wu, and W. B. Song (2008), Three-dimensional MHD modeling of the global corona throughout solar cycle 23, *J. Geophys. Res.*, *113*, A03106, doi:10.1029/2007JA012750.

Jiang, C. W., X. S. Feng, Y. Fan, and C. Xiang (2011), Reconstruction of the coronal magnetic field using the CESE-MHD method, *Astrophys. J.*, *727*, 101.

Jiang, C. W., X. S. Feng, S. T. Wu, and Q. Hu (2012), Study of the three-dimensional coronal magnetic cield of active region 11117 around the time of a conned flare using a data-driven CESE-MHD model, *Astrophys. J.*, *759*, 85.

Jiang, C. W., X. S. Feng, S. T. Wu, and Q. Hu (2013), Magnetohydrodynamic simulation of a sigmoid eruption of active region 11283, *Astrophys. J.*, *771*, L30.

Jiang, C. W., S. T. Wu, X. S. Feng, and Q. Hu (2014a), Formation and eruption of an active region sigmoid. I. A study by nonlinear force-free modeling, *Astrophys. J.*, *780*, 55.

Jiang, C., S. T. Wu, X. Feng, and Q. Hu (2014b), Nonlinear force-free field extrapolation of a coronal magnetic flux rope supporting a large-scale solar filament from a photospheric vector magnetogram, *Astrophys. J.*, *786*, L16.

Kliem, B., and T. Török (2006), Torus instability, *Phys. Rev. Lett.*, *96*(25), 255002, doi:10.1103/PhysRevLett.96.255002.

Li, G., G. P. Zank, and W. K. M. Rice (2003), Energetic particle acceleration and transport at coronal mass ejection-driven shocks, *J. Geophys. Res.*, *108*(A2), 1082, doi: 10.1029/2002JA009666.

Li, G., G. P. Zank, and W. K. M. Rice (2005), Acceleration and transport of heavy ions at coronal mass ejection-driven shocks, *J. Geophys. Res.*, *110*, A06104, doi:10.1029/2004JA010600.

Li, G., G. P. Zank, O. Verkhoglyadova, R. A. Mewaldt, C. M. S. Cohen, G. M. Mason, and M. I. Desai (2009), Shock geometry and spectral breaks in large SEP events, *Astrophys. J.*, *702*, 998–1004.

Li, G., R. Moore, R. A. Mewaldt, L. Zhao, and A. W. Labrador (2012), A twin-CME scenario for ground level enhancement events, *Space Sci. Rev.*, *171*, 141–160.

Liou, K., C.-C. Wu, M. Dryer, S.-T. Wu, D. B. Berdichevsky, S. Plunkett, R. A. Mewaldt, and G. M. Mason (2013), Magnetohydrodynamic fast shocks and their realtion to solar energetic particle event intensities, *Terr. Atmos. Oceanic Sci.*, *24*(2), 165–173, doi:10.3319/TAO.2012.05.08.01.

Liou, K., C.-C. Wu, M. Dryer, S.-T. Wu, N. Rich, S. Plunkett, L. Simpson, C. D. Fry, and K. Schenk (2014), Global hybrid simulation of extremely fast coronal mass ejection on 23 July 2012, *J. Atmos. Sol. Terr. Phys.*, *121*, 32–41.

Lu, G. D., et al. (1998), Global energy disposition during the January 1997 magnetic cloud event, *J. Geophys. Res.*, *103*(A6), 11,685–11,694, doi:10.1029/98JA00897.

Lugaz, N., I. I. Roussev, I. V. Sokolov, and C. Jacobs (2010), Solar terrestrial simulations of CMEs with a realistic initiation mechanism: Case study for active region 10069, *AIP Conf. Proc.*, *1216*, 440–443.

Luhmann, J. G., Y. Li, C. N. Arge, P. R. Gazis, and R. Ulrich (2002), Solar cycle changes in coronal holes and space weather cycles, *J. Geophys. Res.*,*107*(A8), 1154, doi:10.1029/2001JA007550.

Manchester, W. B., IV, T. I. Gombosi, I. Roussev, D. L. De Zeeuw, I. V. Sokolov, K. G. Powell, and G. Toth (2004a), Three-dimensional MHD simulation of a flux rope driven CME, *J. Geophys. Res.*, *109*, A01102, doi:10.1029/2002JA009672.

Manchester, W. B., IV, T. I. Gombosi, I. Roussev, A. Ridley, D. L. De Zeeuw, I. V. Sokolov, K. G. Powell, and G. Toth (2004b), Modeling a space weather event from the Sun to the Earth: CME generation and interplanetary propagation, *J. Geophys. Res.*, *109*, A02107, doi:10.1029/2003JA010150.

Manchester, W. B., IV, A. Vourlidas, G. Toth, N. Lugaz, I. I. Roussev, I. V. Sokolov, T. I. Gombosi, D. L. De Zeeuw, and M. Opher (2008), Three dimensional MHD simulation of the 2003 October 28 coronal mass ejection: Comparison with LASCO coronagraph observations, *Astrophys. J.*, *684*, 1448–1460.

Mikić, Z., and J. A. Linker (1994), Disruption of coronal magnetic arcades, *Astrophys. J.*, *430*, 898–912.

Odstrcil, D., and V. J. Pizzo (2009), Numerical heliospheric simulations as assisting tool for interpretation of observations by STEREO heliospheric imagers, *Sol. Phys.*, *259*, 297–309.

Pagano, P., D. H. Mackay, and S. Poedts (2013), Magnetohydrodynamic simulations of the ejection of a magnetic flux rope, *Astron. Astrophys.*, *554*, A77.

Plunkett, S., and S. T. Wu (2000), Coronal mass ejections (CME) and their goeeffectiveness, *IEEE Trans. Plasma Sci.*, *28*(6), 1807–1817.

Reames, D. V. (1999), Particle acceleration at the Sun and in the heliosphere, *Space Sci. Rev.*, *90*, 413–491.

Reames, D. V. (2009), Solar energetic-particle release times in historic ground-level events, *Astrophys. J.*, *706*, 844.

Roussev, I. I., I. V. Sokolov, T. G. Forbes, T. L. Bombosi, M. A. Lee, and J. I. Sakai (2004), A numerical model of a corona mass ejection: shock development with implications for the acceleration of GeV protons, *Astrophys. J.*, *605*, L73–L76.

Shen, F., X. S. Feng, S. T. Wu, and C. Q. Xiang (2007), Three-dimensional MHD simulation of CMEs in three-dimensional background solar wind with self-consistent structure on the source surface as input: Numerical simulation of the January 1997 Sun-Earth connection event, *J. Geophys. Res.*, *112*, A06109, doi:10.1029/2006JA012164.

Shen, F., X. S. Feng, S. T. Wu, C. Q. Xaing, and W. B. Song (2011), Three-dimensional MHD simulation of the evolution of the April 2000 CME event and its induced shocks using a magnetized plasma blob model, *J. Geophys. Res.*, *116*, A04102, doi:10.1029/2010JA015809.

Shen, F., S. T. Wu, X. S. Feng, and C.-C. Wu (2012), Acceleration & deceleration of coronal mass ejections during propagation and interaction, *J. Geophys. Res.*, *117*, A11101, doi:10.1029/2012JA017776.

Toth, G., D. L. De Zeeuw, T. I. Gombosi, W. B. Manchester, A. J. Ridley, I. V. Sokolov, and I. I. Roussev (2007), Sun-to-thermosphere simulation of the 28–30 October 2003 storm with the Space Weather Modeling Framework, *Space Weather*, *5*, S06003, doi:10.1029/2006SW00272.

Van der Vorst, H. A. (1992), Bi-CGSTAB: A fast and smoothly converging variant of Bi-CG for the solution of nonsymetric linear systems, *SIAM J. Sci. Stat. Comput.*, *13*(2), 631.

Vandas, M., S. Fischer, P. Pelant, M. Dryer, Z. Smith, and T. Detman (1998), Propagation of a spheromak: 2. Three-dimensional structure of a spheromak, *J. Geophys. Res.*, *103*(A10), 23,717–23,725, doi:10.1029/98JA01902.

Vourlidas, A., B. J. Lynch, R. A. Howard, and Y. Li (2013), How many CMEs have flux ropes? Deciphering the signatures of shocks, flux ropes, and prominences in coronagraph observations of CMEs, *Sol. Phys.*, *284*, 179–201.

Wang, A. H., S. T. Wu, E. Tandberg-Hanssen, and F. Hill (2011), Utilization of multiple measurements for global three-dimensional magnetohydrodynamic simulations, *Astrophys. J.*, *732*, 19.

Webb, D. F. (2013), Coronal mass ejections and space weather, in *International Symposium on Solar Terrestrial Physics*, *ASI Conf. Ser.*, vol. 10, edited by N. Gopalswamy et al., pp. 37–49, Astron. Soc. of India, Bangalore, India.

Wood, B. E., C.-C. Wu, A. P. Rouillard, R. A. Howard, and D. G. Socker (2012), A coronal holes's effects on CME shock morphology in the inner heliosphere, *Astrophys. J.*, *755*, 43.

Wu, C.-C., and R. P. Lepping (2015a), Comparisons of characteristics of magnetic clouds and cloud-like structures during 1995–2012, *Sol. Phys.*, *290*, 1243–1269.

Wu, C.-C., and R. P. Lepping (2015b), Relationships among geomagnetic storms, interplanetary shocks, magnetic clouds, and sunspot number during 1995–2012, *Sol. Phys.*, *291*, 265–284, doi:10.1007/s11207-015-0806-9.

Wu, C.-C., X. S. Feng, S. T. Wu, M. Dryer, and C. D. Fry (2006), Effects of the interaction and evolution of interplanetary shocks on "background" solar wind speeds, *J. Geophys. Res.*, *111*, A12104, doi:10.1029/2006JA011615.

Wu, C.-C., C. D. Fry, S. T. Wu, M. Dryer, and K. Liou (2007), Three-dimensional global simulation of ICME propagation from the Sun to the heliosphere: 12 May 1997 solar event, *J. Geophys. Res.*, *112*, A09104, doi:10.1029/2006JA012211.

Wu, C.-C., D. Murray, S. T. Wu, W. Brian, C. D. Fry, K. Liou, and S. Plunkett (2011), Global three-dimensional simulation of the interplanetary evolution of the observed geoeffective CME during the epoch August 1–4, 2010, *J. Geophys. Res.*, *116*, A12103, doi:10.1029/2011JA016947.

Wu, C.-C., K. Liou, A. Vourlidas, S. Plunkett, M. Dryer, S. T. Wu, and R. A. Mewald (2015), Global magnetohydrodynamic simulation of the March 15, 2013 coronal mass ejection event-interpretation of the 30–80 MeV proton flux, *J. Geophys. Res. Space Physics*, *121*, doi:10.1002/2015JA021051.

Wu, S. T., and J. F. Wang (1987), Numerical tests of a modified full-implicit-continuous-eulerian (FICE) scheme with projected normal characteristic boundary conditions for MHD flows, *Comput. Methods Appl. Mech. Eng.*, *64*, 267–282.

Wu, S. T., and M. Dryer (2015), Comparative analyses of current three-dimensional numerical solar wind models, *Sci. China Earth Sci.*, *58*(6), 839–858.

Wu, S. T., W. P. Guo, D. J. Michels, and L. F. Burlaga (1999), MHD description of the dynamical relationships between a flux-rope, streamer, coronal mass ejection (CME) and magnetic cloud: An analysis of the 1997 January Sun-Earth connection event, *J. Geophys. Res.*, *104*(A7), 14,789–14,801, doi:10.1029/1999JA900099.

Wu, S. T., W. P. Guo, S. P. Plunkett, B. Schmieder, and G. M. Simnett (2000), Coronal mass ejections (CMEs) initiation: Models and observations, *J. Atmos. Sol. Terr. Phys.*, *62*, 1489–1498.

Wu, S. T., H. N. Zheng, S. Wang, B. J. Thompson, S. P. Plunkett, X. P. Zhao, and M. Dryer (2001), Three-dimensional numerical simulation of MHD waves observed by the extreme ultraviolet imaging telescope, *J. Geophys. Res.*, *106*(A11), 25,089–25,102, doi:10.1029/2000JA000447.

Wu, S. T., T. X. Zhang, E. Tandberg-Hanssen, Y. Liu, X. S. Feng, and A. Tan (2005), Numerical magnetohydrodynamic experiments for testing the physical mechanisms of coronal mass ejections acceleration, *Sol. Phys.*, *225*, 157–175.

Wu, S. T., A. H. Wang, L. Yang, and J. Todd Hoeksema (2006), Data driven magnetohydrodynamic (MHD) model for active region (AR) evolution, *Astrophys. J.*, *652*, 800.

Wu, S. T., C. W. Jiang, X. S. Feng, Q. Hu, and Y. Liu (2013), Simulation of sigmoid and filament eruption of AR11283 using a 3D data-driven magnetohydrodynamic model, in *Proceedings of IAU Symposium*, vol. 300, edited by B. Schmieder, J.-M. Malherbe, and S. T. Wu, Cambridge Univ. Press, Cambridge, U. K.

Yang, L. P., X. S. Feng, C. Q. Xiang, Y. Liu, X. P. Zhao, and S. T. Wu (2012), Time-dependent MHD modeling of the global solar corona for year 2007: Driven by daily-updated magnetic field synoptic data, *J. Geophys. Res.*, *117*, A08110, doi:10.1029/2011JA017494.

Zank, G. P., W. K. M. Rice, and C. C. Wu (2000), Particle acceleration and coronal mass ejection driven shocks: A theoretical model, *J. Geophys. Res.*, *105*(A11), 25,079–25,095, doi:10.1029/1999JA000455.

Zhang, T. X., and S. T. Wu (2009), Magnetohydrodynamic simulation of non-flux rope coronal mass ejections, *J. Geophys. Res.*, *114*, A05107, doi:10.1029/2008JA013860.

Zhou, Y. F., and X. S. Feng (2013), MHD numerical study of the latitudinal deflection of coronal mass ejection, *J. Geophys. Res. Space Physics*, *118*, 6007–6018, doi:10.1002/2013JA018976.

Zhou, Y. F., X. S. Feng, S. T. Wu, D. Du, F. Shen, and C. Q. Xiang (2012), Using 3D spherical plasmoid to interpret the Sun-to-Earth propagation of 4 November 1997 coronal mass ejection event, *J. Geophys. Res.*, *117*, A01102, doi:10.1029/2010JA016380.

Zhou, Y. F., X. S. Feng, and X. H. Zhao (2014), Using a 3-D MHD simulation to interpret propagation and evolution of a coronal mass ejection observed by multiple spacecraft: The 3 April 2010 event, *J. Geophys. Res. Space Physics*, *119*, 9321–9333, doi:10.1002/2014JA020347.